

Structural aspects of asymptotically safe black holes

Benjamin Koch* and Frank Saueressig**

*Pontificia Universidad Católica de Chile,
Av. Vicuña Mackenna 4860,
Santiago, Chile

**Radboud University Nijmegen,
Institute for Mathematics, Astrophysics and Particle Physics (IMAPP),
Heyendaalseweg 135, 6525 AJ Nijmegen, The Netherlands

Abstract. We study the quantum modifications of classical, spherically symmetric Schwarzschild (Anti-) de Sitter black holes within Quantum Einstein Gravity. The quantum effects are incorporated through the running coupling constants G_k and Λ_k , computed within the exact renormalization group approach, and a common scale-setting procedure. We find that, in contrast to common intuition, it is actually the cosmological constant that determines the short-distance structure of the RG-improved black hole: in the asymptotic UV the structure of the quantum solutions is universal and given by the classical Schwarzschild-de Sitter solution, entailing a self-similarity between the classical and quantum regime. As a consequence asymptotically safe black holes evaporate completely and no Planck-size remnants are formed. Moreover, the thermodynamic entropy of the critical Nariai-black hole is shown to agree with the microstate count based on the effective average action, suggesting that the entropy originates from quantum fluctuations around the mean-field geometry.

PACS numbers: 04.62.+v, 03.65.Ta

1. Introduction

Black holes [1, 2] are perhaps the most fascinating objects known to exist in the universe. In particular, they provide an important testing ground for physics involving strong gravitational fields. Within classical general relativity, the simplest class of black holes are given by a Schwarzschild black hole, embedded in either Minkowski- or (Anti-)de Sitter space. These arise as static, spherical symmetric solutions of Einsteins equations in the presence of a cosmological constant and are completely characterized by the value of Newtons constant, the cosmological constant and their mass, appearing as a free constant of integration. As a common feature the solutions share a space-like singularity at the center of the black hole.

Understanding the dynamics of the black hole spacetime when quantum effects of the geometry are switched on, constitutes an important challenge in theoretical physics. In particular, they provide an important laboratory for testing gravitational theories that go beyond classical general relativity. At the semi-classical level this has led to the discovery of exciting phenomena including the evaporation of a black hole due to Hawking radiation and, more general, the development black hole thermodynamics. It also nurtured the idea that a full quantum treatment of a black hole could resolve the curvature singularity lurking at its center.

Clearly, questions concerning the resolution of the black hole singularity, the final state of the black hole evaporation or the microscopic origin of the black hole entropy should be addressed within a consistent theory of quantum gravity. In this work we will investigate these questions within the effective average action approach [3] to Weinberg's Asymptotic Safety scenario [4], see [5, 6, 7, 8, 9] for current reviews. The key ingredient in this scenario is a non-Gaussian fixed point (NGFP) of the gravitational RG-flow which provides the UV-completion of gravity at trans-Planckian energies. By now, the properties of this fixed point have been studied in a series of works first approximating Γ_k by the Einstein-Hilbert action [10, 11, 12, 13, 14] and subsequently adding higher derivative terms [15, 16, 17, 18, 19, 20, 21, 22] and the square of the Weyl-tensor [23, 24, 25]. Furthermore, quantum effects in the ghost sector have been studied in [26] and RG-flows including surface terms have been considered in [27]. As a key common result, all these works found a NGFP of the gravitational theory space suitable for Asymptotic Safety. Following [9], we will call the resulting quantum theory of gravity Quantum Einstein Gravity (QEG).

The phenomenological consequences of Asymptotic Safety are most conveniently explored based on the gravitational effective average action $\Gamma_k[g_{\mu\nu}]$ [3]. In a nutshell, $\Gamma_k[g_{\mu\nu}]$ is constructed in such a way that, when evaluated at tree level, it describes gravitational phenomena, *including quantum corrections*, whose typical momenta are of the order k . Subsequently, this property has been used to study quantum corrections to classical space-times by including the effect of scale-dependent coupling constants either at the level of the classical solutions, classical equations of motion, or the Lagrangian density and subsequently identifying k with a physical cutoff scale of the system.

Starting from the pioneering works [28, 29], these techniques have been used to explore quantum-modifications of classical Schwarzschild black holes [30, 31, 32, 33, 34, 35] and black holes including angular momentum [36, 37]. The inclusion of higher-derivative terms has been considered in [38] while the reverse-engineering of the RG-improved black hole geometry based on thermodynamical properties has been undergone in [39]. Finally, the creation of asymptotically safe black holes in gravitational theories with large extra dimensions has been studied in [40, 41, 42, 43] and conditions on the formation of a singularity based on the RG-improved collapse of a thin matter shell have been derived [44]. These works find that the NGFP underlying Asymptotic Safety indeed has significant consequences for the emergent structure of the quantum-improved black holes. For the Schwarzschild case, the quantum corrections either soften the spatial singularity encountered in the interior of the black hole or remove it entirely [29]. Even more striking, the quantum-improvement significantly affects the semi-classical black hole evaporation process. Instead of evaporating completely, the temperature of the quantum-improved black hole drops to zero at a finite mass, suggesting that the final state of the black hole evaporation is a Planck-mass remnant [29].

The novel feature of the present work is the inclusion of a running cosmological constant in the RG-improvement procedure. This step is inevitable in a consistent implementation of the RG-flow: even if one sets $\Lambda_k = 0$ at one fixed scale k , the RG-flow will generate a non-vanishing cosmological constant dynamically. In particular the dimensionless cosmological constant at the NGFP is positive, λ_* , entailing that the dimensionful counterpart Λ_k will diverge quadratically at high energies. Thus it is a priori unclear that setting $\Lambda_k = 0$, an approximation that underlies all previous RG-studies of black holes, is a good approximation. In fact, we will show that including the running of Λ drastically modifies the picture of black holes in Asymptotic Safety. While counter-intuitive at first sight, the cosmological constant has a crucial effect on resolution of the black hole singularity and the black hole evaporation process. Moreover, it opens up new insights on the origin of the black hole entropy within Asymptotic Safety.

The rest of this work is organized as follows. Sects. 2 and 3 review the properties of classical, spherical symmetric black hole solutions incorporating a non-trivial cosmological constant and the RG-flow of QEG in the Einstein-Hilbert truncation, respectively. This discussion provides the basis for introducing our RG-improvement procedure in Sect. 4. The properties of the resulting quantum-improved black hole solutions are investigated in Sects. 5 (short distance structure), 6 (global structure of the solutions), and 7 (thermodynamic properties), respectively. In Sect. 8 we summarize our results by highlighting the improvement-scheme dependent and independent conclusions. Appendix A finally contains complementing information on improved actions and improved equations of motions.

2. Classical black hole solutions with cosmological constant

We start with the discussion of classical static and spherical symmetric black hole solutions in the presence of a cosmological constant. These solutions are well-known and correspond to the line-element

$$ds^2 = -f(r) dt^2 + f(r)^{-1} dr^2 + r^2 d\Omega_2^2 \quad (1)$$

with

$$f(r) = 1 - \frac{2GM}{r} - \frac{1}{3} \Lambda r^2. \quad (2)$$

Here G and Λ denote the classical Newton constant and cosmological constant, $d\Omega_2^2$ is the volume element of the two-sphere, and M is an integration constant. Depending on the sign of Λ , the line-element describes a Schwarzschild-AdS ($\Lambda < 0$), Schwarzschild ($\Lambda = 0$), or Schwarzschild-dS ($\Lambda > 0$) black hole, respectively.

This class of solutions possesses a space-like singularity at $r = 0$. This can be made visible by computing the square of the Riemann tensor, which is independent of the choice of coordinates

$$R_{\mu\nu\rho\sigma} R^{\mu\nu\rho\sigma} = \frac{48G^2 M^2}{r^6} + \frac{8\Lambda^2}{3}. \quad (3)$$

Moreover, the black hole solutions give rise to horizons where (2) vanishes. Multiplying $f(r)$ by r , the roots of the cubic equation can be found analytically,

$$r_0 = -\mathcal{R}^{-1/3} - \frac{1}{\Lambda} \mathcal{R}^{1/3}, \quad (4)$$

and

$$r_{\pm} = \frac{1}{2} \left(1 \pm i\sqrt{3} \right) \mathcal{R}^{-1/3} + \frac{1 \mp i\sqrt{3}}{2\Lambda} \mathcal{R}^{1/3}. \quad (5)$$

Here

$$\mathcal{R} = 3GM\Lambda^2 + \sqrt{9G^2 M^2 \Lambda^4 - \Lambda^3}. \quad (6)$$

These roots constitute a black hole horizon if the resulting r is real and positive. The actual horizon structure of the black holes therefore depends on the sign of Λ and M and can be determined from the determinant of the cubic $rf(r)$. For $\Lambda < 0$ there is a single real root,

$$r_{\text{AdS}} \equiv r_0, \quad (7)$$

while r_{\pm} constitutes a complex pair. Thus the Schwarzschild-AdS black hole has a single black hole horizon. For $\Lambda = 0$ this horizon agrees with the one of the Schwarzschild black hole $r_{\text{SS}} = 2GM$.

For Schwarzschild-dS black holes, $\Lambda > 0$, the situation is slightly more complicated. For $M = 0$, the line element (1) reduces to dS space with a cosmological horizon at

$$r_c = \sqrt{3/\Lambda} = r_+|_{M=0}. \quad (8)$$

For $M > 0$ a black hole horizon emerges at

$$\tilde{r} \equiv r_-. \quad (9)$$

For increasing M , the black hole horizon grows while the cosmological horizon $r_c \equiv r_+$ shrinks. For the critical mass

$$M_{\max} \equiv \frac{1}{3G\sqrt{\Lambda}} \quad (10)$$

the two horizons coincide and one obtains the Nariai black hole as the maximal black hole in dS space. For $M > M_{\max}$ the two horizons disappear and the line-element (1) describes a naked singularity.

Given a horizon situated at r_H , one can determine its thermodynamic properties foremost the Hawking temperature

$$T_H = \frac{\partial_r f(r)}{4\pi} \Big|_{r=r_H} \quad (11)$$

and the Beckenstein-Hawking entropy

$$S = \frac{\pi r_H^2}{G}. \quad (12)$$

For the Schwarzschild-dS black holes, which will play a central role in our investigation, the thermodynamics of the two horizons has been discussed extensively in the context of the dS/CFT correspondence [45, 46]. The cosmological horizon r_c has Hawking temperature and entropy

$$T_c = \frac{1}{4\pi r_c} (\Lambda r_c^2 - 1), \quad S_c = \frac{\pi r_c^2}{G}, \quad (13)$$

while the evaluation of (11) and (12) at the black hole horizon \tilde{r} gives

$$\tilde{T} = \frac{1}{4\pi \tilde{r}} (1 - \Lambda \tilde{r}^2), \quad \tilde{S} = \frac{\pi \tilde{r}^2}{G}. \quad (14)$$

Remarkably, the entropy associated with both the cosmological and black hole horizon can be expressed through a Cardy-Verlinde formula [45, 46] which is conjectured to capture the entropy of a conformal field theory (CFT) valid in arbitrary dimension [47]. This provides a strong hint that the thermodynamics of the Schwarzschild-dS black hole has the correct entropy to be described by a CFT.

For the cosmological horizon this equivalence can be shown as follows. Using a surface-counterterm method, the gravitational mass of the Schwarzschild-dS black hole was determined in [48, 49]

$$E = -M = \frac{r_c}{2G_N} \left(\frac{1}{3} \Lambda r_c^2 - 1 \right). \quad (15)$$

which expresses the mass M of the black hole in terms of the radius of the cosmological horizon. The Casimir energy E_c , defined as the non-extensive part of (15), $E_c \equiv 3E - 2TS$ is given by [45]

$$E_c = -\frac{r_c}{G} \quad (16)$$

Given the relations (15) and (16) it is straightforward to verify that the entropy S_c can be cast into Cardy-Verlinde form

$$S_c = \pi \sqrt{\frac{3}{\Lambda}} \sqrt{|E_c|(2E - E_c)}. \quad (17)$$

Similarly, \tilde{S} , eq. (14), also follows the Cardy-Verlinde formula, provided that one adopts the mass definition of Abbott and Deser [50]

$$\tilde{E} = M = \frac{\tilde{r}}{2G} \left(1 - \frac{1}{3} \Lambda \tilde{r}^2 \right). \quad (18)$$

In this case the definition of the Casimir energy yields

$$\tilde{E}_c = \frac{\tilde{r}}{G} \quad (19)$$

and the extensive part of the energy is

$$2\tilde{E} - \tilde{E}_c = -\frac{\Lambda}{3G} \tilde{r}^3. \quad (20)$$

Given these quantities, it is straightforward to check that

$$\tilde{S} = \pi \sqrt{\frac{3}{\Lambda}} \sqrt{E_{c,+} |2E_+ - E_{c,+}|} \quad (21)$$

also takes the form of a Cardy-Verlinde formula. This suggests that both the black hole horizon and the cosmological horizon have the correct thermodynamics for a dual description in terms of a dual CFT in the framework of the dS/CFT correspondence. These results will become important when discussing the properties of the quantum-improved black holes in Sect. 5.

3. RG-flows in Quantum Einstein Gravity

The Asymptotic Safety program encodes the quantum effects in a the scale dependent gravitational effective average action $\Gamma_k[g, \xi, \bar{\xi}; \bar{g}]$, which satisfies the exact functional renormalization group equation (FRGE) [3]

$$\partial_k \Gamma_k[g, \xi, \bar{\xi}; \bar{g}] = \frac{1}{2} \text{Tr} \left[\left(\Gamma_k^{(2)} + \mathcal{R}_k \right)^{-1} \partial_k \mathcal{R}_k \right]. \quad (22)$$

Here $g_{\mu\nu}$ is the averaged metric, $\bar{g}_{\mu\nu}$ an unspecified background metric, and $\xi, \bar{\xi}$ are the ghost fields. Moreover $\Gamma_k^{(2)}$ is the second variation of Γ_k with respect to the fluctuation fields at fixed background. The crucial ingredient in (22) is the infrared cutoff \mathcal{R}_k which provides a k -dependent mass-term for fluctuations with momenta $p^2 \gg k^2$. It renders the trace-contribution finite and peaked at $p^2 \approx k^2$. The solutions of the FRGE interpolate between the bare action at $k \rightarrow \infty$ and the effective action $\Gamma[g] = \Gamma_{k=0}[g, 0, 0; \bar{g}]|_{g=\bar{g}}$ by integrating out quantum fluctuations shell-by-shell in momentum space. In this sense the object $\Gamma_k[g, 0, 0; \bar{g}] \equiv \Gamma_k[g]$ provides an effective description of the physics at momentum scale k . Its vertices include all quantum corrections from fluctuations with $p^2 > k^2$, while long-range fluctuations are untouched. This property is central for using $\Gamma_k[g]$ for an effective description of the quantum physics.

While it is impossible to solve the FRGE exactly, it can still be used to gain insights on the quantum nature of physical processes by projecting the exact RG-flow onto subspaces spanned by a suitable ansatz for Γ_k . For the study of (A)dS black holes

conducted in this work, we thereby restrict ourselves to the Einstein-Hilbert truncation where the gravitational part of Γ_k is of (euclidean) Einstein-Hilbert form

$$\Gamma_k^{\text{grav}}[g] = \frac{1}{16\pi G_k} \int d^4x \sqrt{g} [-R + 2\Lambda_k] \quad (23)$$

and includes two scale-dependent couplings, Newton's constant G_k and the cosmological constant Λ_k . The beta functions resulting from this truncation have first been derived in [3] and are most conveniently expressed in terms of the dimensionless coupling constants

$$g_k = G_k k^2 \quad , \quad \lambda_k = \Lambda_k k^{-2} \quad . \quad (24)$$

In terms of g_k and λ_k the RG equations become a system of autonomous differential equations

$$k\partial_k g_k = \beta_g(g_k, \lambda_k) \quad , \quad k\partial_k \lambda_k = \beta_\lambda(g_k, \lambda_k) \quad , \quad (25)$$

where

$$\beta_\lambda(g, \lambda) = (\eta_N - 2)\lambda + \frac{1}{2\pi} g \left[10\Phi_2^1(-2\lambda) - 8\Phi_2^1(0) - 5\eta_N \tilde{\Phi}_2^1(-2\lambda) \right] \quad , \quad (26)$$

$$\beta_g(g, \lambda) = (2 + \eta_N)g \quad . \quad (27)$$

The anomalous dimension of Newton's constant η_N is given by

$$\eta_N(g, \lambda) = \frac{gB_1(\lambda)}{1 - gB_2(\lambda)} \quad , \quad (28)$$

with the following functions of the dimensionless cosmological constant

$$B_1(\lambda) \equiv \frac{1}{3\pi} \left[5\Phi_1^1(-2\lambda) - 18\Phi_2^2(-2\lambda) - 4\Phi_1^1(0) - 6\Phi_2^2(0) \right] \quad , \quad (29)$$

$$B_2(\lambda) \equiv -\frac{1}{6\pi} \left[5\tilde{\Phi}_1^1(-2\lambda) - 18\tilde{\Phi}_2^2(-2\lambda) \right] \quad . \quad (30)$$

The threshold functions Φ and $\tilde{\Phi}$ are defined in [3] and encode the dependence of the beta functions on the IR-regulator \mathcal{R}_k . For most applications, it is convenient to work with the non-differentiable 'optimized cutoff' [14] where

$$\Phi_n^p(w) = \frac{1}{\Gamma(n+1)} \frac{1}{1+w} \quad , \quad \tilde{\Phi}_n^p(w) = \frac{1}{\Gamma(n+2)} \frac{1}{1+w} \quad . \quad (31)$$

The phase diagram resulting from the flow (25) has been constructed in [13] and is shown in Fig. 1. The flow is governed by the interplay of a Gaussian fixed point (GFP) located at the origin, $g_* = 0, \lambda_* = 0$ and an NGFP which, for the cutoff (31), is located at

$$\lambda_* = 0.193 \quad , \quad g_* = 0.707 \quad , \quad g_*\lambda_* = 0.137 \quad . \quad (32)$$

Besides the coordinates of the NGFP, we also give the value of the product $g_*\lambda_*$ which was argued to be observable [12] and its RG-scheme dependence is significantly suppressed in comparison with the single quantities g_* and λ_* alone.

The NGFP acts as an UV-attractor for all RG-trajectories shown in the upper half-plane. Thus it governs the behavior of gravity at high energies and provides its UV-completion. Since the dimensionless couplings approach constant values, the NGFP

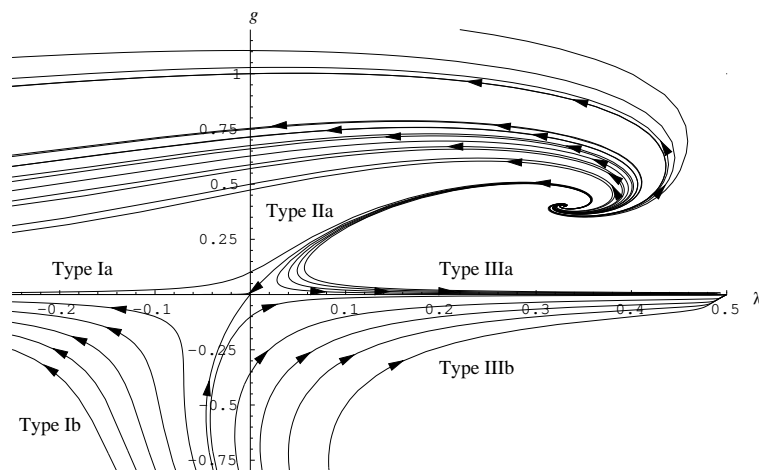


Figure 1: RG flow originating from the Einstein-Hilbert truncation (25) obtained with a sharp cut-off. The arrows point in the direction of increasing coarse-graining, i.e. of decreasing k . From [13].

also fixes the scaling behavior of the dimensionful Newton's constant and cosmological constant at high energies. Inverting (24) we obtain

$$\lim_{k \rightarrow \infty} G_k = g_* k^{-2}, \quad \lim_{k \rightarrow \infty} \Lambda_k = \lambda_* k^2. \quad (33)$$

Following the RG-flow towards the IR there is a crossover. Depending on whether the flow passes to the left, right, or ends at the GFP, the low-energy limit is given by classical general relativity with a negative (Type Ia), positive (Type IIIa) or zero (Type IIa, Separatrix) value of the cosmological constant.

Based on the flow pattern shown in Fig. 1, it is a plausible assumption that the NGFP will govern the structure of black holes at short distances. The universality entailed by the fixed point then lets us expect that black hole solutions which at long distances correspond to classical AdS, dS, and Schwarzschild black holes actually possess the same short distance structure. The scaling relations (24) together with the fixed point condition then indicates that the value of the dimensionful cosmological constant actually becomes sizable *at short distances*, indicating that in terms of RG-improved processes one should not restrict oneself to the study of Schwarzschild black holes, setting $\Lambda_k = 0$ throughout, but work in a more general class of black hole solutions which also capture the effect of the cosmological constant. In fact, it is this generalization that underlies the novel insights in this paper and will thoroughly modify the picture of black holes in Asymptotic Safety.

For the purpose of studying the phenomenological consequences of the RG flow depicted in Fig. 1, it is convenient to work with approximations of the RG trajectory that can be captured by analytic expressions. Here we will make use of the analytical curves [51]

$$g(k) = \frac{G_0 k^2}{1 + k^2/g_*}, \quad (34)$$

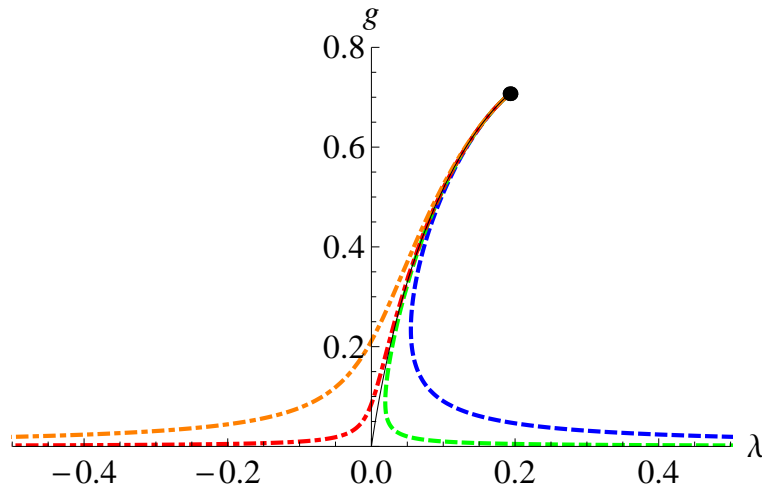


Figure 2: Analytic approximation of the RG trajectories shown in Fig. 1, provided by the parametric curves (35), (34) for $G_0 = 1$, $\Lambda_0 = -0.01$ (orange), $\Lambda_0 = -0.001$ (red), $\Lambda_0 = 0$ (black), $\Lambda_0 = 0.001$ (green), $\Lambda_0 = 0.01$ (blue). The position of the NGFP (32) is marked by the black dot.

$$\lambda(g) = \frac{g_* \lambda_*}{g} \left(\left(5 + \frac{\Lambda_0 G_0}{g_* \lambda_*} \right) [1 - g/g_*]^{3/2} - 5 + 3g/(2g_*)(5 - g/g_*) \right). \quad (35)$$

Here the position of the NGFP (32) constitutes an input parameter and the type and details of the RG trajectory can be dialed by specifying the IR-values of Newton's constant G_0 and the cosmological constant Λ_0 . For some illustrative choices of these parameters, the resulting parametric curves are shown in Fig. 2. Comparing Figs. 1 and 2 we readily observe that the analytically approximated curves describe the global transition from the UV to the IR. The feature that the analytic approximation does not capture is the spiraling of the RG flow around the NGFP. At this stage, we stress that none of the results found in the sequel depend on the detailed properties of the RG trajectories. In particular, the modeling of the RG trajectories is not essential when studying how the gravitational RG flow affects classical black hole solutions at short distances.

4. Scale setting in RG-improvement schemes

At this stage we want to exploit the information on the gravitational RG-flow to gain insights on the structure of black holes in Asymptotic Safety. For this purpose we apply the RG-improvement procedure, first used by Bonanno and Reuter for classical Schwarzschild black holes [29], to the classical black hole solutions (1). At the present stage, we limit ourselves to the discussion of improving the classical solutions. The case of improved equations of motion and improved actions give rise to similar results and are covered in Appendix B.

The basic idea underlying our RG-improvement scheme is to start from the classical

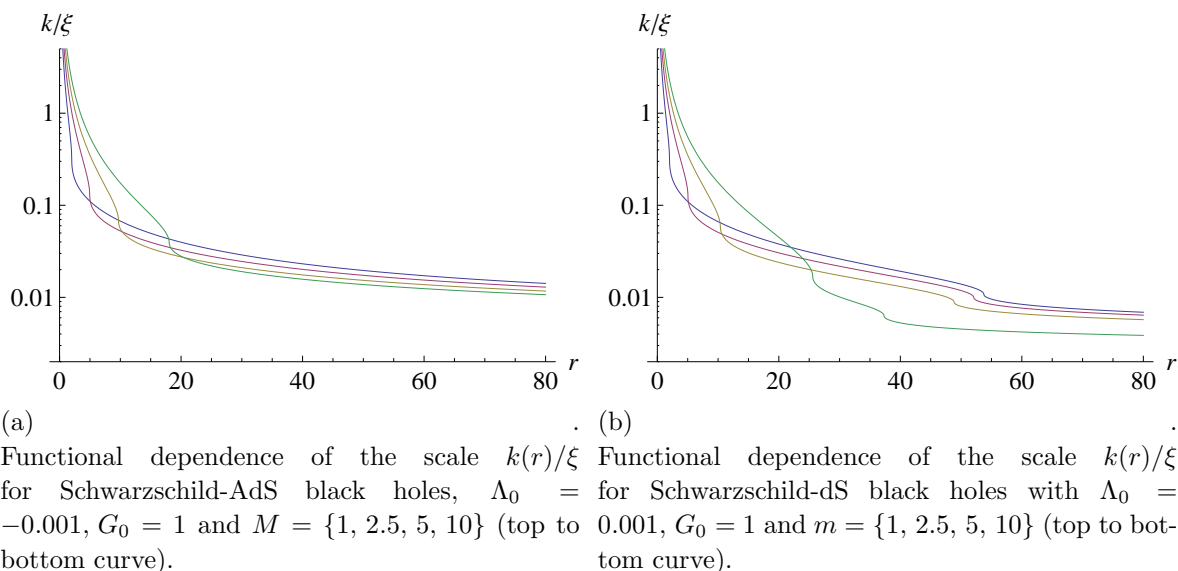


Figure 3: Cutoff-identification $k(r)$ resulting from identifying $d(r)$ with the radial geodesic distance (37).

solution (1) and promote the coupling constants to running couplings, $G \rightarrow G_k, \Lambda \rightarrow \Lambda_k$, whose scale-dependence is governed by the beta-functions (26). The RG-improvement procedure then relates the RG-scale k with a physical cutoff scale. Following the arguments in [29] this cutoff-identification should be a coordinate invariant statement and preserve the symmetries of the classical solution. The symmetry requirement then fixes $k \equiv k(r)$ while the first condition of coordinate invariance can be incorporated by constructing $k(r)$ from a geodesic quantity. This leads to the form

$$k(P(r)) = \frac{\xi}{d(P(r))} \quad , \quad (36)$$

where $d(P)$ is the distance scale which provides the relevant cutoff k when the test particle is located at the point P . The constant ξ is expected to be of order unity and has to be fixed by using a physics argument. In the context of RG-improved Schwarzschild black holes, several choices for $d(r)$ have been advocated in the literature. Here we will identify $d(P)$ with the radial proper distance from the center of the black hole to the point P along a purely radial curve \mathcal{C}_r

$$d(r) = \int_{\mathcal{C}_r} \sqrt{|ds^2|} \quad . \quad (37)$$

For a given classical (A)dS black hole solution, specified through G, Λ, M , the function $d(r)$ can easily be found numerically. For two particular examples the resulting cutoff identification $k(r)$ is shown in Fig. 3. The first observation is that the relation between r and k is actually monotonic, i.e., large values of the momentum cutoff correspond to short distances and vice versa. This constitutes an important prerequisite for the feasibility of the proposed cutoff identification. Moreover, we observe that the cutoff-identification contains points where the slope actually becomes infinite. These points

correspond to the horizons of the black holes, where the line-element degenerates, even though the geodesic distance remains finite. In the AdS case the black holes have only one horizon located at (4). For the Schwarzschild-dS black holes there are two such points associated with the black hole and cosmological horizons given by (5). As expected from the discussion in Sect. 2, the two horizons of the Schwarzschild-dS black hole approach each other for increasing mass M .

Besides having the full numerical cutoff-identification at our disposal, it is also useful to obtain analytic expressions for $k(r)$ valid in the deep UV and deep IR. For short distances, $r \rightarrow 0$ this function can be expanded in a series in r whose leading terms are easily calculated analytically

$$d(r) \simeq \frac{2}{3} \frac{1}{\sqrt{2GM}} r^{3/2} \left(1 + \frac{3}{10} \frac{r}{2GM} + \mathcal{O}(r^2) \right). \quad (38)$$

The short distance behavior is completely fixed by G and M . In particular the cosmological constant enters into the cubic term of the bracket only, and is thus not important in this regime. The cosmological constant is, however, crucial for the large distance behavior of the cutoff-identification. Depending on the sign of Λ the leading large-distance behavior (approximated by setting $M = 0$ in (1)) is

$$d(r) \simeq \begin{cases} \sqrt{\frac{3}{\Lambda}} \arcsin \left(\sqrt{\frac{\Lambda}{3}} r \right), & \Lambda > 0 \\ r, & \Lambda = 0 \\ \sqrt{\frac{3}{-\Lambda}} \operatorname{arcsinh} \left(\sqrt{-\frac{\Lambda}{3}} r \right), & \Lambda < 0 \end{cases}. \quad (39)$$

For $\Lambda > 0$ the geodesic distance becomes maximal at a finite value $r^2 = 3/\Lambda$ indicating the presence of the cosmological horizon.

As an alternative to the scale-setting procedure based on the proper distance introduced in equation (37), Appendix A discusses a proper-time improvement where the cutoff is identified with the proper time measured by a freely falling observer. This scheme has the virtue that the resulting cutoff identification is smooth at the black hole horizon. The detailed investigation of this alternative, carried out in Appendix A, establishes that all conclusions drawn from the proper-distance improvement remain valid when applying this alternative scale-setting procedure, pointing at the robustness of the results.

5. RG-improved black hole solutions in the UV

In this section, we will RG-improve the classical Schwarzschild-(A)dS black hole solutions (2) in order to investigate how the NGFP, eq. (32), affects the short-distance structure of the black holes. Following the discussion of Sect. 4, we start from the classical solution and promote the coupling constants to scale-dependent quantities

$$f_k(r) = 1 - \frac{2MG_k}{r} - \frac{1}{3} \Lambda_k r^2. \quad (40)$$

In the deep UV, $k \rightarrow \infty$, the scale dependence of the coupling constants is governed by the NGFP. Substituting the fixed point scaling (33), into the radial function (40) one gets

$$f_*(r) = 1 - \frac{2Mg_*}{k^2 r} - \frac{1}{3} (\lambda_* k^2) r^2. \quad (41)$$

Here g_* , λ_* denote the position of the NGFP and the $*$ acts as a reminder that this solution describes the asymptotics for $k \rightarrow \infty$.

In the next step we perform the cutoff-identification (36), relating k to the radial geodesic distance. In the UV the identification is given by

$$k(r) \simeq \frac{3}{2} \sqrt{2G_0 M} \xi r^{-3/2}. \quad (42)$$

Here G_0 indicates the IR-value of Newton's constant at $k = 0$. Substituting this asymptotics into (41) it is straightforward to obtain the RG-improved line-element *valid at the NGFP*

$$f_*(r) = 1 - \frac{2G_0 M}{r} \left(\frac{3}{4} \lambda_* \xi^2 \right) - \frac{1}{3} \left(\frac{4g_*}{3G_0 \xi^2} \right) r^2. \quad (43)$$

Most remarkably, the RG-improved function $f_*(r)$ valid at high energies is *self-similar* to the classical solution (2). Promoting k to a function of r interchanges the terms containing Newton's constant and the cosmological constant so that the actual r -dependence remains the same. Note that the inclusion of the cosmological constant term is crucial for this self-similarity to work.

Requiring that the classical and RG-improved solution both give rise to the same asymptotic cutoff identification (42) fixes the numerical constant ξ ,

$$\xi_{\text{sc}}^2 = \frac{4}{3\lambda_*}. \quad (44)$$

For this particular value the RG-improvement scheme becomes self-consistent and we will use this criterion to fix the a priori free numerical constant ξ , if not stated otherwise. Setting $\xi = \xi_{\text{sc}}$, we obtain the line-element for the self-consistent RG-improved black hole solution valid in the non Gaussian fixed point regime

$$f_{*,\text{sc}}(r) = 1 - \frac{2G_0 M}{r} - \frac{1}{3} \Lambda_{\text{eff}} r^2, \quad (45)$$

with the effective cosmological constant

$$\Lambda_{\text{eff}} = \frac{g_* \lambda_*}{G_0}. \quad (46)$$

Notably, the dimensionality of Λ_{eff} (valid in the UV) is set by the square of the Planck mass $M_{\text{Pl}}^2 \equiv G_0^{-1}$, while its magnitude (in Planck units) is governed by the universal dimensionless product $g_* \lambda_*$. This product cannot be chosen by hand, but constitutes a prediction from Asymptotic Safety. Its magnitude has been computed in a number of works $g_* \lambda_* \approx 0.1$ [9, 52].

A direct consequence of the self-similarity between the classical line-element (1) and its RG-improved counterpart (43) is that both metrics give rise to the same singular

behavior at $r = 0$. The square of the Riemann-tensor computed from the RG-improved metric is

$$R_{\mu\nu\rho\sigma}R^{\mu\nu\rho\sigma} = \frac{48G_0^2M^2}{r^6} \left(\frac{3}{4} \lambda_* \xi^2 \right)^2 + \frac{8}{3} \left(\frac{4g_*}{3G_0\xi^2} \right)^2. \quad (47)$$

Thus the RG-improvement *does not resolve* the spatial singularity at $r = 0$. This is in contrast to earlier investigations of RG-improved Schwarzschild black holes carried out by Bonanno and Reuter [29, 31], which reported the resolution of the singularity due to the RG improvement. This apparent mismatch is resolved by noting that the latter computation has essentially been carried out at $\lambda_* = 0$. Setting $\lambda_* = 0$ in (43), the RG-improved line-element is the one of classical de Sitter-space so that there is no singularity at the origin. This can also be confirmed from (47) which becomes regular at $r = 0$ once we set $\lambda_* = 0$. At this stage, it is worthwhile stressing that the singularity appearing in this expression is not caused by the Newton's constant, but rather counter intuitively originates from the inclusion of the cosmological constant. The non-zero and positive value of the latter is an intrinsic feature of the NGFP underlying Asymptotic Safety and thus cannot be avoided.

6. RG-improved black hole solutions: global structure

Following the discussion of the previous section we will extend our investigation to the whole interval $0 \leq r < \infty$ and develop the global picture of the RG improved (A)dS black holes. Our starting point is again the k -dependent line-element (40). Instead of working with the asymptotic scaling of the coupling constants where $g_k = g_*$, $\lambda_k = \lambda_*$, the k -dependence of the dimensionless couplings is captured by the analytic approximation of the RG-trajectory (34, 35), however. Subsequently, the scale-identification is performed by replacing $k \mapsto k(r)$ with the function $k(r)$ shown in Fig. 3. The resulting RG-improved functions $f(r)$ are then shown in Fig. 4. Comparing the classical (dashed) and RG-improved (solid) solutions for the same values M , one first observes that for $r \ll M$ and $r \gg M$ the curves actually agree with a very high precision. For small r this behavior actually reflects the self-similarity of the classical and improved solution discovered in the last section. The precise matching of the asymptotics thereby hinges on setting $\xi = \xi_{\text{sc}}$ since this choice also implies an agreement in the numerical coefficients fixing the short-distance behavior.

The quantum effects captured by the RG-improvement are then restricted to the intermediate regime where $G_k M/r \approx 1$. From Fig. 4 we see, that these modifications are rather small, however. In particular they do not affect the horizon structure of the black holes. For the AdS and dS-case the (inner) black hole horizon \tilde{r} is slightly shifted to smaller values,

$$\tilde{r}_{\text{imp}} \lesssim \tilde{r}_{\text{class}}, \quad (48)$$

while the cosmological horizon essentially retains its position. The shift of the inner black hole horizon could be interpreted as shielding of the bare mass parameter

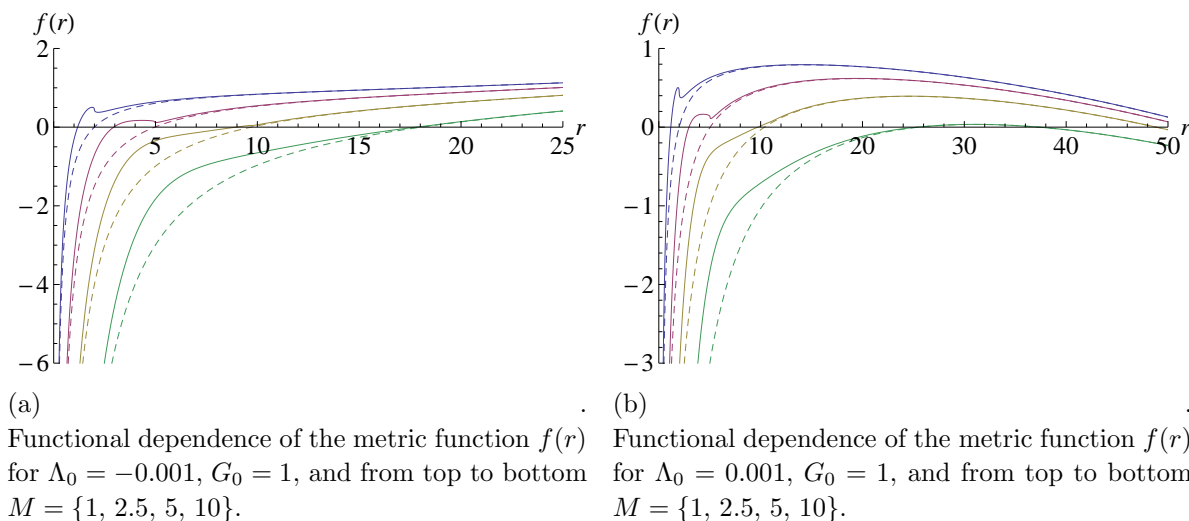


Figure 4: Radial dependence of the RG-improved metric function $f(r)$ for $\xi = \xi_{\text{sc}}$. The dashed lines correspond to the classical solutions while the solid lines correspond to the improved solution.

due to quantum gravity corrections. This behavior agrees with earlier findings [29]. Furthermore, also the RG-improved Schwarzschild-dS black holes possess a maximal mass for which the black hole and cosmological horizons coincide. For our illustrative example this mass agrees with the mass of the classical Nariai mass (10) to very high precision

$$M_{\text{max,imp}} \simeq \frac{1}{3G_0\sqrt{\Lambda_0}} = 10.54, \quad (49)$$

where the same values of G_0 and Λ_0 were used as in previous graphics.

So far, we have discussed RG-improved black hole solutions for one particular choice of the cutoff-identification, setting $\xi = \xi_{\text{sc}}$. While this value is distinguished by the self-consistency of the RG-improvement scheme, it is worthwhile to investigate in as much the results shown in Fig. 4 depend on this choice. Our focus is thereby on “light” black holes with mass around the Planck mass. For a typical Schwarzschild-AdS black hole the parametric dependence of the improved $f_k(r)$ on ξ is illustrated in Fig. 5. The figure illustrates that there is the possibility that the RG-improved solutions develop an additional pair of horizons if ξ is chosen sufficiently small. These horizons emerge at intermediate scales $M/r \approx 1$. The asymptotic behavior of the solutions for $M/r \gg 1$ and $M/r \ll 1$ is, however, independent of the choice of ξ .

The emergence of a new pair of horizons is investigated more thoroughly in Fig. 6. The numerical study reveals, that this feature only occurs, if the black hole under consideration is sufficiently light, $M \leq M_{\text{crit}}$. For the class of Schwarzschild-(A)dS black holes with $\Lambda_0 = \pm 0.001$ the critical mass has been obtained numerically and is given by

$$\text{AdS :} \quad \Lambda_0 = -0.001 \quad M_{\text{crit}} = 2.94 \quad (50)$$

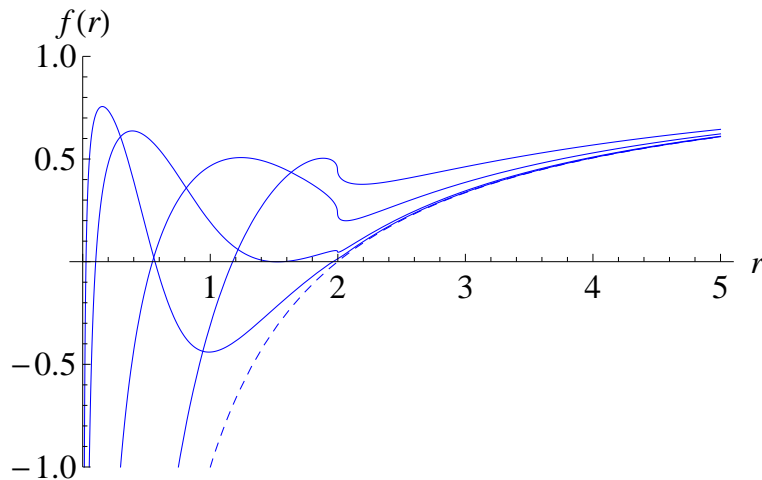


Figure 5: Functional dependence of the metric function $f(r)$ on the RG-improvement parameter for a prototypical light Schwarzschild-AdS black hole with $M = 1$, $\Lambda_0 = -0.001$, $G_0 = 1$. From top to bottom, the curves are obtained for $\xi = \{\xi_{\text{sc}}, 1.5, 0.6, 0.3\}$. The classical result (dashed line) is included for comparison.

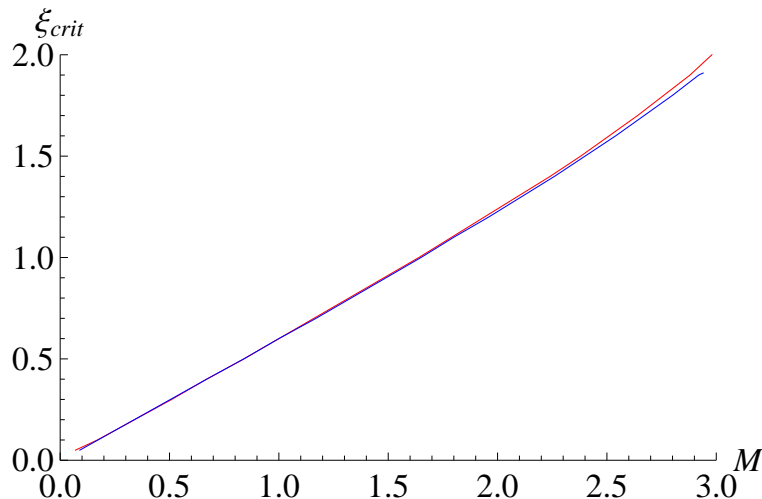


Figure 6: Critical value of the RG-improvement parameter ξ for $\Lambda_0 = 0.001$ (red curve) and $\Lambda_0 = -0.001$ (blue curve) and $G_0 = 1$. For $\xi \leq \xi_{\text{crit}}$ a light RG-improved black hole develops an additional pair of horizons. For masses $M > M_{\text{crit}}$ no additional horizons are formed, independently of the actual value of ξ .

$$\text{dS} : \quad \Lambda_0 = 0.001 \quad M_{\text{crit}} = 2.98 . \quad (51)$$

For masses $M \leq M_{\text{crit}}$ one then finds a critical value of the RG-improvement parameter $\xi_{\text{crit}}(M)$ for which the horizon structure changes. The resulting function $\xi_{\text{crit}}(M)$ is shown in Fig. 6 and depends only weakly on the IR-value of the cosmological constant. For black holes with mass $M > M_{\text{crit}}$ no additional pair of horizons is formed, independently of the actual value of the RG-improvement parameter. In particular for the distinguished RG-parameter ξ_{sc} the horizon structure of the RG-improved solution

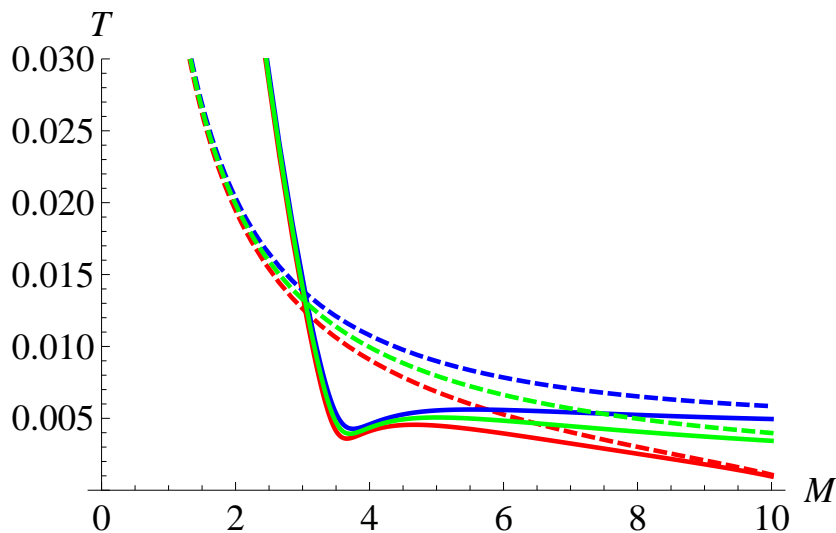


Figure 7: Temperature of the RG-improved (inner) black hole horizon based on a classical IR value of the cosmological constant given by $\Lambda_0 = -0.001$ (top blue curve), $\Lambda_0 = 0$ (green curve in the middle), and $\Lambda_0 = 0.001$ (red curve bottom) and $G_0 = 1$. The temperature of the corresponding classical black hole is given by the dashed lines for comparison.

is always the one found in the classical case, independently of the actual mass of the black hole.

7. RG-improved black hole solutions: thermodynamics

After determining the horizon structure of the RG-improved black hole solutions we now investigate the resulting thermodynamical properties. We start with discussing the general black hole evaporation process, before investigating the entropy of the microscopic black holes of Sect. 7.1 in more detail in Sect. 7.2. Throughout the section we fix $\xi = \xi_{sc}$.

7.1. Black hole evaporation

The black hole evaporation process is controlled by the inner horizon. The temperature associated with this horizon is given by (11). For a given RG-improved solution with fixed Λ_0, G_0 this expression can easily be evaluated numerically. The resulting temperature as a function of the mass-parameter M is shown in Fig. 7.

The figure illustrates, that for very massive black holes, $M\sqrt{G_0} \gg 1$, the temperature of the classical and RG-improved solutions actually coincide. The quantum corrections from the RG-improvement set in once the mass of the black hole becomes comparable to the Planck mass $M\sqrt{G_0} \simeq 1$. In this regime the temperature of the improved black hole is actually lower than in the classical case, and for a given window situated around the horizon of the classical black hole, actually decreases with

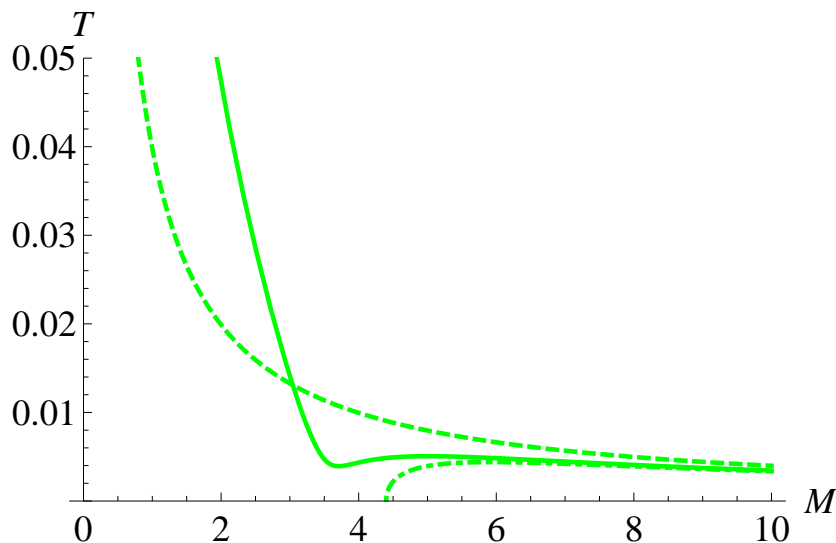


Figure 8: Comparison between the temperatures of the (RG-improved) Schwarzschild black hole with $\Lambda_0 = 0$ depending on its mass. The classical behavior is given by the dashed (upper) curve. The RG-improved solution obtained by Bonanno and Reuter [29] (setting $\Lambda_k = 0$ throughout) is given by the dash-dotted (lower) curve while the horizon temperature obtained from including the running of Λ_k is given by the solid curve.

decreasing mass M . Below this window the temperature increases rapidly, so that the sub-Planckian black holes are actually hotter than their classical counterparts. For light black holes, the final part of the temperature curve is universal in the sense that it is completely controlled by the properties of the NGFP (32). In particular it is independent of the IR-value Λ_0 , so that the final stage of the evaporation process is actually independent whether one considers an asymptotically Schwarzschild or (A)dS black hole.

At this stage, it is illustrative to compare our findings with the RG-improved solutions [29], which approximated $\Lambda_k = 0$ throughout. The temperature of the resulting RG-improved Schwarzschild black holes are shown in Fig. 8. Comparing the solid curve with the dashed-dotted curve obtained from $\Lambda_k = 0$ it is again illustrated that the running cosmological constant plays a crucial role for the thermodynamics of microscopic black holes with mass below the Planck-mass. In particular the inclusion of Λ_k prevents that the temperature of the inner horizon drops to zero at a finite mass M . Thus the RG-improved black hole solutions evaporate completely, once the scale-dependence of Λ_k is taken into account and our analysis indicates that there is no formation of Planck-mass black hole remnants within Asymptotic Safety.

7.2. State count for microscopic black holes

We close this section with the computation of the entropy (21) associated with the inner horizon of the quantum-improved Schwarzschild-dS black hole constructed in Sect. 5.

Comparing the RG-improved radial function (43) and its classical analogue (2) shows that the entropy of the inner horizon is again of the form (14) with the replacement $G \mapsto G_0 \left(\frac{3}{4}\lambda_*\xi^2\right)$. Substituting the inner black hole radius $\tilde{r} = r_-$, determined by evaluating (5) for the RG-improved solution (43), then yields

$$\tilde{S}_* = \frac{4\pi}{g_*\lambda_*} \cos^2\left(\frac{1}{3}(\pi + \theta)\right). \quad (52)$$

Here

$$\theta \equiv \arctan\left(\sqrt{\frac{4}{27\tilde{m}^2} - 1}\right). \quad (53)$$

All the RG-improvement scheme dependence can be absorbed into the rescaled mass parameter

$$\tilde{m} = M\xi\sqrt{G_0}\sqrt{g_*}\lambda_*. \quad (54)$$

The formulas hold for $0 \leq \tilde{m}^2 \leq 4/27$. The upper bound corresponds to the Nariai black hole with critical mass eq. (10). For $\tilde{m}^2 > 4/27$ the horizons vanish and there is a naked singularity. This entails that the quantum improved black hole has a ξ -independent maximal entropy that is purely determined by the universal product $g_*\lambda_*$. Setting $\theta = 0$ the maximal entropy of the black hole horizon is

$$\tilde{S}_{\max} = \frac{\pi}{g_*\lambda_*}. \quad (55)$$

Notice that, in this limit the black hole and cosmological horizons actually coincide so that the total entropy of the black hole is given by twice the black hole horizon entropy. As a crosscheck, one can use the explicit values of the fixed point coordinate to translate the critical mass into the physical mass measured in terms of the Planck mass

$$M_{\max}|_{\xi=\xi_{\text{sc}}} = 0.90M_{\text{Pl}}. \quad (56)$$

Thus the analysis holds for microscopic black holes with masses around the Planck mass or below.

Most remarkably, the entropy (55) can also be obtained by counting the microstates of the Nariai black holes. This counting can be carried out by exploiting the ‘state counting’ property of the effective average action [27]

$$\ln \mathbb{Z}_k \equiv -\Gamma_k[g]|_{g=g_{\text{sol}}}, \quad (57)$$

where $\Gamma_k[g]$ is to be evaluated at the running self-consistent background. At the level of the truncation (23), g_{sol} is just the solution of the scale-dependent equations of motion resulting from (23). The scale-dependent partition function $\ln \mathbb{Z}_k$ then counts the field modes integrated out between $k = \infty$ and the IR-scale k .

The Euclidean instanton solutions describing the Nariai black hole have already been studied in detail [53, 54, 55] and correspond to the Einstein spaces with topology $S^2 \times S^2$. Their line-element is given by

$$ds^2 = \frac{1}{\Lambda_k} \left(d\theta_1^2 + \sin^2\theta_1 d\varphi_1^2 + d\theta_2^2 + \sin^2\theta_2 d\varphi_2^2 \right). \quad (58)$$

Here the scale-dependent cosmological constant reflects that the instanton is the solution solves the equations of motion obtained from the scale-dependent Γ_k . Evaluating the action (23) of the instanton, one obtains

$$\ln \mathbb{Z}_k = -\Gamma_k[g]|_{g=S^2 \times S^2} = \frac{2\pi}{G_k \Lambda_k}, \quad (59)$$

where we used that the volume of the unit two-sphere is given by $\text{Vol}(S^2) = 4\pi$. The entropy (55) actually holds on the NGFP. Taking the limit $k \rightarrow \infty$ of (59), we finally obtain

$$\ln \mathbb{Z}_* = \frac{2\pi}{g_* \lambda_*}. \quad (60)$$

Remarkably, $\ln \mathbb{Z}_* = 2\tilde{S}_{\text{max}}$ and thus agrees with the total entropy of the two horizons of the Nariai black hole. Thus the state counting formula provides a microscopic derivation of the thermodynamic entropy (55). We stress that the result (60) is actually independent of any RG-improvement procedure and solely relies on the Euclidean instanton action and the existence of the fixed . The matching between the entropy \tilde{S}_* and the microstate count suggests that the pertinent degrees of freedom underlying the thermodynamics of the black hole are the *geometry fluctuations around the background geometry*.

8. Summary and Conclusions

In this work we have analyzed the structure and thermodynamics of static, spherical symmetric black holes in Quantum Einstein Gravity. In this course we applied the RG-improvement techniques pioneered by Bonanno and Reuter [28, 29] and subsequently refined by several groups [30, 42, 33, 44] to the classical black hole solutions. The crucial novel feature of our analysis is the inclusion of the scale-dependent cosmological constant Λ_k . As illustrated in Fig. 1, Λ_k is always generated dynamically even if the cosmological constant is zero at one particular RG scale. As it was shown in the main text, the inclusion of the running cosmological constant drastically affects on the structure of the quantum-improved black holes *at short distances*.

At first sight, the modification of short-distance physics due the cosmological constant seems rather counterintuitive since Λ is typically connected to gravity phenomena at long distances. In Quantum Einstein Gravity (QEG) the UV-completion of gravity is however provided by a non-Gaussian fixed point of the theories RG flow, implying that the *dimensionless couplings* of the theory become constant at high energies. For the *dimensionful* Newton's constant and cosmological constant this entails

$$\lim_{k \rightarrow \infty} G_k = g_* k^{-2} \rightarrow 0, \quad \lim_{k \rightarrow \infty} \Lambda_k = \lambda_* k^2 \rightarrow \infty, \quad (61)$$

providing a first heuristic argument that at high energies the cosmological constant could be of the same importance as Newtons constant. Formulated differently, at the non-Gaussian fixed point behaves “highly quantum”, so that it is a priori unclear that our

classical intuition still holds. In fact, our analysis establishes a picture of the quantum-improved black holes which drastically differs from previous QEG studies setting $\Lambda_k = 0$ throughout, even though both rely on the same computational method.

The results of our study of static, spherical symmetric black holes within the Einstein-Hilbert approximation of QEG can be summarized as follows:

a) **The role of the cosmological constant**

Including the effect of a scale-dependent cosmological constant in the RG-improvement process drastically affects the structure of the quantum-improved black holes *at short distances*. Thus a consistent RG-improvement procedure requires working in the class of Schwarzschild-(A)dS solutions of Einsteins equations.

b) **Universal short distance behavior**

The short-distance structure of all quantum-improved black holes is governed by the non-Gaussian RG fixed point. This entails that the structure of light black holes is universal. In particular it is independently of the IR-value of Newtons constant and the cosmological constant and therefore identical for classical Schwarzschild, Schwarzschild-dS and Schwarzschild-AdS black holes.

c) **Curvature singularities**

In the presence of the cosmological constant, the curvature singularity at $r = 0$ is not resolved.

The results a) to c) hold independent of the actual RG-improvement scheme. Moreover, we made the following, RG-improvement scheme-dependent observations:

d) **Distinguished RG-improvement scheme**

In the main text we focused on a particular RG-improvement scheme (initially proposed in [29]) which relates the RG-scale k to the radial geodesic distance of a point P to the origin. This scheme is singled out by the fact that it is self-consistent in the UV: Both the classical and RG-improved solutions give rise to the same cutoff-identification. Moreover, results are consistent with applying the RG-improvement at the level of the equations of motion and flowing action Γ_k and to the alternative choice of geodesic distance examined in Appendix A.

e) **Classical-quantum black hole duality**

Working within this distinguished RG-improvement scheme, the quantum-improved microscopic black holes are described by the *classical Schwarzschild-dS solution*. In the improvement process the cosmological constant and Newton's constant actually swap places, so that it is λ_* that actually controls the short distance behavior of the solution while g_* takes over the role of the classical cosmological constant term.

f) **Black hole evaporation and remnant formation**

The inclusion of the cosmological constant leads to a complete evaporation of the asymptotically safe black holes. In particular there is no mechanism any more that enforces the formation of Planck-mass remnants which implies that naked

singularities formed by the radiating quantum-improved black holes. The final stage of the evaporation process is universal and governed by the properties of the non-Gaussian fixed point which determines the temperature of the inner horizon of the microscopic black holes.

g) **Microstate count**

For the Nariai black hole, appearing in a particular limit of the quantum-improved black hole solutions in the deep UV, the thermodynamic entropy of the black hole configuration agrees with the microscopic state count based on the effective average action. This matching suggests that the degrees of freedom responsible for the black hole entropy are quantum fluctuations around the mean-field black hole configuration and constitutes the first microscopic derivation of a thermodynamical entropy within Asymptotic Safety.

Notably, all of these conclusions remain valid when performing the proper-time cutoff identification advocated in Appendix A, adding further evidence for their robustness.

In particular the result e) opens up new perspectives on black holes in Asymptotic Safety. On one hand the emerging picture is reminiscent of the classicalization scenario advocated in [56], which proposes that the effective degrees of freedom of gravity at high energies are given by classical black hole solutions. The observation that the asymptotically safe black holes are self-similar in the sense that the quantum-improved black holes found by evaluating the RG-improvement at the non-Gaussian fixed point are again described by the classical Schwarzschild-dS solution may hint at a hitherto unnoticed connection between these ideas.

A second profound consequence of the observation that the quantum-improved black holes found at the non-Gaussian fixed point are actually Schwarzschild-dS is that their entropy can be expressed in terms of the Cardy-Verlinde formula [57], which is conjectured to describe the entropy of a CFT in general dimension [47]. This, in particular, dismisses the arguments [58] that entropy count of Asymptotic Safety is not compatible with the one expected from a CFT. Moreover, it opens up the exciting possibility that there is a description of the quantum-black hole geometry on the basis of the dS/CFT correspondence [59].

Finally, we expect that the analysis of more complex black hole solutions including electromagnetic charges and angular momentum will also be affected by our findings. In particular, the evaporation of asymptotically safe black holes in theories with large extra dimensions [40, 41, 42, 43] may be altered by the inclusion of the cosmological constant. We leave the investigation of these point to future works.

Acknowledgements

We thank M. Reuter for helpful discussions and an anonymous referee for suggesting the proper time improvement studied in Appendix A. F.S. thanks the Pontificia Universidad Católica de Chile (Santiago) for hospitality during the initial stage of the project. The work of B.K. was supported proj. Fondecyt 1120360 and anillo Atlas Andino 10201

while the research of F.S. is supported by the Deutsche Forschungsgemeinschaft (DFG) within the Emmy-Noether program (Grant SA/1975 1-1).

Appendix A. Proper time RG improvement

In this section we will study an alternative choice for the scale-setting procedure (36). In this case, the scale k is identified with the inverse of the proper time measured by a freely falling observer starting at rest at r_0 and reaching the classical black hole singularity after the time τ . We will call this novel RG-improvement scheme proper-time improvement (pti). The main advantage of this procedure is that it leads to a cutoff identification that is smooth when passing through a horizon, thereby eliminating the points with infinite slope appearing in Figure 3. As the main result of this appendix, we establish that all conclusions listed in the summary are confirmed by this alternative RG-improvement scheme.

We start by deriving the proper time interval $\tau(r_0)$ passing on the clock of a freely falling observer starting at rest at r_0 before reaching the black hole singularity at $r = 0$. For the Schwarzschild solution this computation can, e.g., be found in [64] and it is straight forward to generalize it to the case with a cosmological constant. Starting from the geodesic equation derived from the classical line element (2), one first establishes from the time component that

$$E = \left(1 - \frac{2GM}{r} - \frac{\Lambda r^2}{3}\right)u^0, \quad (\text{A.1})$$

with $u^\nu = dx^\nu/d\tau$ denoting the observers four-velocity, is a conserved quantity. Evaluated for the observer at rest at r_0 the energy can be computed explicitly

$$E^2 = \left(1 - \frac{2GM}{r_0} - \frac{\Lambda r_0^2}{3}\right). \quad (\text{A.2})$$

Using the normalization condition of the four-velocity, $u^\nu u_\nu = -1$, this gives rise to an equation for the radial velocity

$$\frac{dr}{d\tau} = \sqrt{\left(1 - \frac{2GM}{r_0} - \frac{\Lambda}{3}r_0^2\right) - \left(1 - \frac{2GM}{r} - \frac{\Lambda}{3}r^2\right)}. \quad (\text{A.3})$$

The proper time $\tau(r_0)$ depending on the starting point of the observer is obtained by integrating this relation

$$\tau(r_0) = \int_0^{r_0} dr (2GM/r + 1/3\Lambda r^2 - 2GM/r_0 - 1/3\Lambda r_0^2)^{-1/2}. \quad (\text{A.4})$$

The proper-time improvement then uses this expression to related the cutoff scale $k(P(r))$, eq. (36), to the inverse of this expression

$$k(P(r)) = \frac{\xi}{\tau(r)}. \quad (\text{A.5})$$

At this stage, the following remark is in order. For the AdS and Schwarzschild black hole ($\Lambda \leq 0$) this scale-setting procedure provides a good cutoff identification in

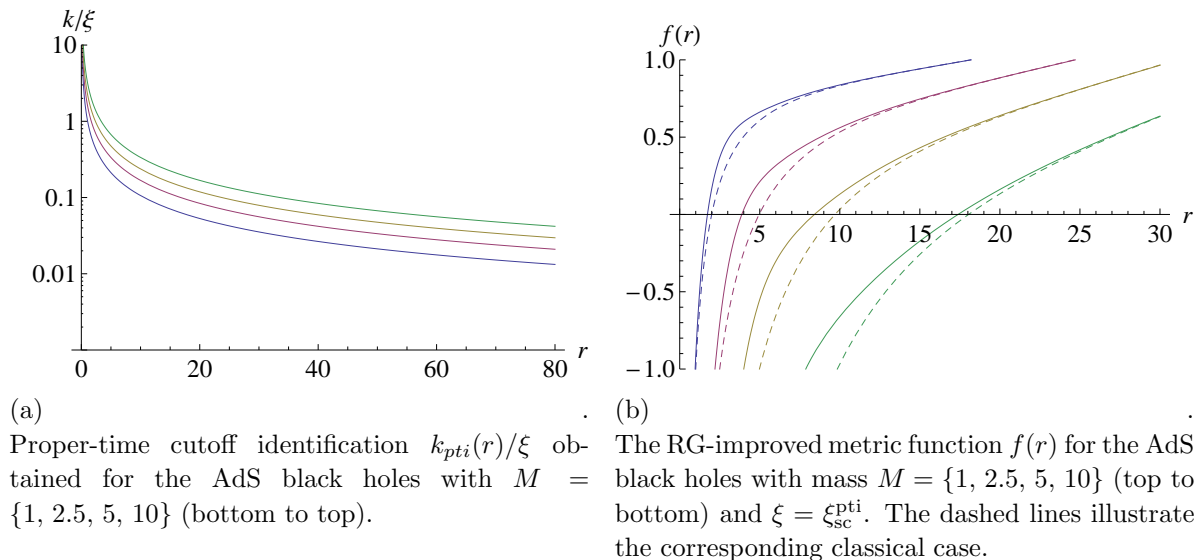


Figure A1: Functional dependence of the scale $k_{pti}(r)/\xi$ (left) and the resulting RG-improved metric factor $f(r)$ (right) for Schwarzschild-AdS black holes with $\Lambda_0 = -0.001$ and $G_0 = 1$.

the sense that $r \rightarrow 0$ corresponds to $k \rightarrow \infty$ and vice versa. For dS black holes, however, the integral (A.4) diverges at a finite radius $r_{tp} = (3GM/\Lambda)^{1/3}$ which is located between the black hole and cosmological horizon of the geometry. Observers starting at $r_0 > r_{tp}$ will not end up in the central black hole singularity. Instead they are falling outward towards the cosmological horizon. Thus, in this case we still have that at short distances $r \rightarrow 0$ implies $k(r) \rightarrow \infty$ while in the IR $k(r) \rightarrow 0$ as $r \rightarrow r_{tp}$. The whole RG-trajectory is therefore evaluated in a finite coordinate interval $r \in [0, r_{tp}]$. This suggests that the proper-time improvement does not lead to a valid cutoff identification in the dS case and we restrict our analysis of global properties to the AdS and Schwarzschild black holes.

When investigating the phenomenological consequences arising from the proper-time improvement scheme, we start with the analysis for small radii. In this case (A.4) can be applied to both the dS and the AdS case. Expanding the integrand of equation (A.4) the short distance asymptotics of $\tau(r)$ is given by

$$\tau(r) = \frac{\pi}{2} \frac{1}{\sqrt{2GM}} r^{3/2} (1 + \mathcal{O}(r)). \quad (\text{A.6})$$

Comparing this result with the short distance expansion (38) shows that both RG-improvement schemes give rise to the *same short distance behavior*. They only differ in a numerical factor which can be reabsorbed in a redefinition of ξ . Thus the UV approximation obtained from the proper-time improvement is identical to the one discussed in section 5, lending further support to the robustness of the results obtained in the main text. In particular there is again a self-consistent solution where

$$\xi_{sc}^{pti} = \frac{3\pi}{4} \xi_{sc}. \quad (\text{A.7})$$

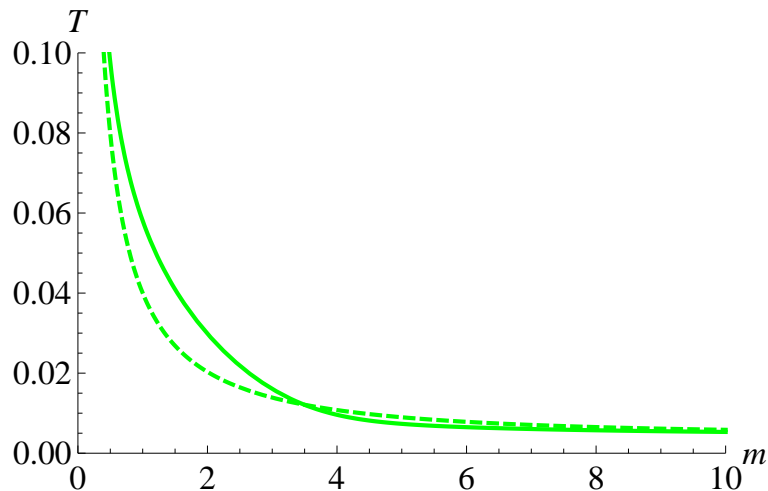


Figure A2: Temperature of the RG-improved AdS black hole with $\Lambda_0 = -0.001$ obtained from the proper-time improvement scheme with $\xi = \xi_{\text{sc}}^{\text{pti}}$. The temperature of the corresponding classical black hole is given by the dashed line for comparison.

For the AdS and Schwarzschild black holes, it also makes sense to discuss the global properties of the RG-improved black hole solutions along the lines of section 6. The cutoff identification $k(r)$ arising from the proper-time improvement is shown in the left diagram of figure A1. Comparing the result to the cutoff identification using the proper distance shown in figure 3 establishes that the schemes give rise to the same asymptotic behavior for small and large values r . Their only difference arises when r is close to the black hole horizon: here the proper-time improvement gives rise to an infinite slope which is smoothed out in the proper-time scheme. As a direct consequence, we find that the RG-improved metric function $f(r)$ for $\xi = \xi_{\text{sc}}^{\text{pti}}$, shown in the right diagram of figure A1 remains monotonic. Decreasing ξ , however, we find that also the proper-time improvement scheme can give rise to additional horizon pairs. In this respect, we recover the global structure of the RG-improved black hole solutions described in section 6.

Following the strategy of section 7, it is also straight forward to obtain the horizon temperature of the RG-improved AdS black hole arising from the proper-time improvement. The result, shown in Figure A2, closely resembles the temperature curve obtained from the RG-improvement based on the proper distance shown in Figure 7. In particular the asymptotics for very small and large masses m are identical. One noticeable difference is that the proper-time improvement leads to a heat-capacity that is strictly negative definite. Since the proper-time improvement is precisely tailored for improving the RG-improvement close to the horizon, we expect, that this actually reflects a genuine property of the RG-improved black hole that is not captured by the proper-distance improvement.

To summarize the results of this appendix, we have found that *all conclusions* summarized in section 8 are also valid for the proper-time improvement scheme. This provides additional evidence for the robustness of the results derived in this work.

Appendix B. Improving equations of motion and action

In this appendix we establish that the quantum-improved solutions constructed in Sect. 5 can also be obtained from other RG-improvement schemes. Their compatibility with “improving the equations of motion” [60] and “improving the action” [61] will be demonstrated in Appendix B.1 and Appendix B.2, respectively.

Appendix B.1. Improving the equations of motion

An alternative route for extracting phenomenological consequences from the running effective average action is the RG-improvement of the equations of motion. In this case the cutoff-identification $k \mapsto k(r)$ is applied at the level of the scale-dependent equations of motion derived from Γ_k . As a consequence, the coupling constants become position-dependent $G_k \mapsto G(x)$ with the dynamics provided by the RG-equations.

For the Einstein-Hilbert ansatz (23) the RG-improved equations of motion read [62]

$$G_{\mu\nu} = -g_{\mu\nu}\Lambda_k + 8\pi G_k T_{\mu\nu} - \Delta t_{\mu\nu}, \quad (\text{B.1})$$

with $G_{\mu\nu} \equiv R_{\mu\nu} - \frac{1}{2}g_{\mu\nu}R$ being the Einstein-tensor. The position-dependent Newton’s constant leads to an additional contribution to the stress energy tensor [62, 1]

$$\Delta t_{\mu\nu} = G_k (g_{\mu\nu} D^2 - D_\mu D_\nu) \frac{1}{G_k}. \quad (\text{B.2})$$

The consistency of eq. (B.1) then allows to determine the cutoff-identification $k = k(r)$ dynamically. Assuming the conservation of the stress-energy tensor

$$T_{\mu\nu}{}^{;\nu} = 0 \quad (\text{B.3})$$

and applying $g_{\mu\nu}{}^{;\nu} = 0$ together with the Bianchi identity

$$G_{\mu\nu}{}^{;\nu} = 0, \quad (\text{B.4})$$

eq. (B.1) implies that [51]

$$R D_\mu \left(\frac{1}{G_k} \right) - 2 D_\mu \left(\frac{\Lambda_k}{G_k} \right) = 0. \quad (\text{B.5})$$

For a given form of the running couplings this equation can be used to determine the cutoff-identification $k(R)$. In general this relation will include arbitrary powers of the curvature which make the equations of motion (B.1) hard to handle. However, this situation simplifies in the deep UV where the scale-dependence of the couplings simplifies to (33). Substituting the scaling relation at the NGFP, (B.5) becomes

$$\frac{\lambda_*}{g_*} (R - 4\lambda_* k^2) (D_\mu k^2) = 0. \quad (\text{B.6})$$

Asking for a non-trivial solution where $D_\mu k^2 \neq 0$ provides the desired relation between k^2 and the scalar curvature

$$k^2 = \frac{R}{4\lambda_*}. \quad (\text{B.7})$$

This confirms the linear dependency between R and k^2 as it is often used in the FRGE literature and also fixes the constant that comes with this proportionality.

We now focus on vacuum solutions of (B.1), setting $T_{\mu\nu} = 0$. Substituting the fixed point scaling (33) and subsequently performing the cutoff-identification (B.7), we obtain the improved equations of motion *valid in the scaling regime of the NGFP*

$$R_{\mu\nu} - \frac{1}{4}g_{\mu\nu}R + \frac{1}{R}(g_{\mu\nu}D^2 - D_\mu D_\nu)R = 0. \quad (\text{B.8})$$

At this stage, it is straightforward to check that (43) also solves these RG-improved equations of motion. Thus we verified that our RG-improved fixed point solution is also compatible with the “improved equations of motion”-scheme.

Appendix B.2. Improving the action

The RG-improvement procedure can also be applied at the level of the scale-dependent Lagrangian density appearing in the effective average action. This procedure is called “improving the action”. We now demonstrate that the solution (43) can also be obtained from this RG-improvement method.

At the NGFP, the (lorentzian) effective average action (23) takes the form

$$\Gamma_*[g] = \frac{1}{16\pi} \int d^4x \sqrt{-g} k^2 g_*^{-1} (R - 2\lambda_* k^2) \quad (\text{B.9})$$

Following the discussion [63], a natural choice for the cutoff-identification is to postulate a linear relation between the renormalization scale and the curvature,

$$k^2 = \xi R, \quad (\text{B.10})$$

which generalizes (B.7) by including an arbitrary proportionality constant. Substituting this relation into (B.9), the RG-improved action becomes quadratic in the curvature scalar

$$\Gamma_* = \frac{\xi}{16\pi g_*} (1 - 2\lambda_* \xi) \int d^4x \sqrt{-g} R^2. \quad (\text{B.11})$$

For any value of $\xi \neq 1/(2\lambda_*)$, the equations of motion resulting from this action are again given by (B.8). This shows the internal consistency of “improving the equations of motion” and “improving the action”. In particular the fixed point solution (43) can be obtained from both procedures. We stress that this consistency would not hold if the cutoff-identification (37) is replaced by setting $k = \xi/r$.

We close this appendix with the following comments. Recently a special solution of (B.1) has been found in terms of the metric and the radius dependent fields $G(r)$ and $\Lambda(r)$ [35]. Whether this solution really reflects effects due to running couplings is however not yet clear. In this light, tracing (B.8) gives

$$3\frac{\square R}{R} = 0, \quad (\text{B.12})$$

which might be useful for finding more general solutions of (B.8). Finally, one might also consider the improved equations of motion (B.1) without the contribution (B.2). This is

however not in the spirit of this work since it would imply a non-zero and non-conserved stress energy tensor for matter.

- [1] S. M. Carroll, *Spacetime and geometry: An introduction to general relativity*, Addison-Wesley, San Francisco, USA, (2004).
- [2] R. M. Wald, *Quantum field theory in curved space-time and black hole thermodynamics*, Chicago Univ. Press, Chicago, USA, (1994).
- [3] M. Reuter, Phys. Rev. D **57**, 971 (1998), hep-th/9605030.
- [4] S. Weinberg in *General Relativity, an Einstein Centenary Survey*, S.W. Hawking and W. Israel (Eds.), Cambridge University Press, 1979; S. Weinberg, hep-th/9702027.
- [5] M. Niedermaier and M. Reuter, Living Rev. Rel. **9**, 5 (2006).
- [6] M. Reuter and F. Saueressig, in *Geometric and Topological Methods for Quantum Field Theory*, H. Ocampo, S. Paycha and A. Vargas (Eds.), Cambridge Univ. Press, Cambridge (2010); arXiv:0708.1317.
- [7] R. Percacci, R. Percacci, in *Approaches to Quantum Gravity: Towards a New Understanding of Space, Time and Matter*, D. Oriti (Ed.), Cambridge Univ. Press, Cambridge (2009); arXiv:0709.3851.
- [8] D. F. Litim, PoS(QG-Ph) **024** (2008); arXiv:0810.3675.
- [9] M. Reuter and F. Saueressig, New J. Phys. **14**, 055022 (2012); arXiv:1202.2274.
- [10] D. Dou and R. Percacci, Class. Quant. Grav. **15**, 3449 (1998); hep-th/9707239.
- [11] W. Souma, Prog. Theor. Phys. **102**, 181 (1999); hep-th/9907027.
- [12] O. Lauscher and M. Reuter, Phys. Rev. D **65**, 025013 (2002); hep-th/0108040.
- [13] M. Reuter and F. Saueressig, Phys. Rev. D **65**, 065016 (2002); hep-th/0110054.
- [14] D. F. Litim, Phys. Rev. Lett. **92**, 201301 (2004); hep-th/0312114.
- [15] O. Lauscher and M. Reuter, Class. Quant. Grav. **19**, 483 (2002); hep-th/0110021.
- [16] O. Lauscher and M. Reuter, Phys. Rev. D **66**, 025026 (2002); hep-th/0205062.
- [17] S. Rechenberger and F. Saueressig, Phys. Rev. D **86**, 024018 (2012); arXiv:1206.0657.
- [18] A. Codello, R. Percacci and C. Rahmede, Int. J. Mod. Phys. A **23**, 143 (2008); arXiv:0705.1769.
- [19] P. F. Machado and F. Saueressig, Phys. Rev. D **77**, 124045 (2008); arXiv:0712.0445.
- [20] A. Bonanno, A. Contillo and R. Percacci, Class. Quant. Grav. **28**, 145026 (2011); arXiv:1006.0192.
- [21] K. Falls, D. F. Litim, K. Nikolakopoulos and C. Rahmede, arXiv:1301.4191.
- [22] N. Christiansen, D. F. Litim, J. M. Pawłowski and A. Rodigast, arXiv:1209.4038.
- [23] D. Benedetti, P. F. Machado and F. Saueressig, Mod. Phys. Lett. A **24**, 2233 (2009); arXiv:0901.2984.
- [24] D. Benedetti, P. F. Machado and F. Saueressig, Nucl. Phys. B **824**, 168 (2010); arXiv:0902.4630.
- [25] M. R. Niedermaier, Phys. Rev. Lett. **103**, 101303 (2009).
- [26] A. Eichhorn, H. Gies and M. M. Scherer, Phys. Rev. D **80**, 104003 (2009); arXiv:0907.1828; K. Groh and F. Saueressig, J. Phys. A **43**, 365403 (2010); arXiv:1001.5032; A. Eichhorn and H. Gies, Phys. Rev. D **81**, 104010 (2010); arXiv:1001.5033. A. Eichhorn, arXiv:1301.0632.
- [27] D. Becker and M. Reuter, JHEP **1207**, 172 (2012), arXiv:1205.3583. D. Becker and M. Reuter, arXiv:1212.4274.
- [28] A. Bonanno and M. Reuter, Phys. Rev. D **60**, 084011 (1999); gr-qc/9811026.
- [29] A. Bonanno and M. Reuter, Phys. Rev. D **62**, 043008 (2000); hep-th/0002196.
- [30] H. Emoto, hep-th/0511075.
- [31] A. Bonanno and M. Reuter, Phys. Rev. D **73**, 083005 (2006); hep-th/0602159.
- [32] B. F. L. Ward, Acta Phys. Polon. B **37**, 1967 (2006); hep-ph/0605054.
- [33] K. Falls, D. F. Litim and A. Raghuraman, Int. J. Mod. Phys. A **27**, 1250019 (2012); arXiv:1002.0260.
- [34] S. Basu and D. Mattingly, Phys. Rev. D **82**, 124017 (2010); arXiv:1006.0718.
- [35] C. Contreras, B. Koch and P. Riosco, arXiv:1303.3892.

- [36] M. Reuter and E. Tuiran, hep-th/0612037.
- [37] M. Reuter and E. Tuiran, Phys. Rev. D **83**, 044041 (2011); arXiv:1009.3528.
- [38] Y.-F. Cai and D. A. Easson, JCAP **1009**, 002 (2010); arXiv:1007.1317.
- [39] K. Falls and D. F. Litim, arXiv:1212.1821.
- [40] J. Hewett and T. Rizzo, JHEP **0712**, 009 (2007); arXiv:0707.3182.
- [41] D. F. Litim and T. Plehn, Phys. Rev. Lett. **100**, 131301 (2008); arXiv:0707.3983.
- [42] B. Koch, Phys. Lett. B **663**, 334 (2008); arXiv:0707.4644.
- [43] T. Burschil and B. Koch, Zh. Eksp. Teor. Fiz. **92**, 219 (2010); arXiv:0912.4517.
- [44] R. Casadio, S. D. H. Hsu and B. Mirza, Phys. Lett. B **695**, 317 (2011); arXiv:1008.2768.
- [45] R.-G. Cai, Phys. Lett. B **525** (2002) 331; hep-th/0111093.
- [46] R.-G. Cai, Nucl. Phys. B **628** (2002) 375; hep-th/0112253.
- [47] E. P. Verlinde, hep-th/0008140.
- [48] V. Balasubramanian, J. de Boer and D. Minic, Phys. Rev. D **65**, 123508 (2002); hep-th/0110108.
- [49] A. M. Ghezelbash and R. B. Mann, JHEP **0201**, 005 (2002); hep-th/0111217.
- [50] L. F. Abbott and S. Deser, Nucl. Phys. B **195**, 76 (1982).
- [51] B. Koch and I. Ramirez, Class. Quant. Grav. **28**, 055008 (2011); arXiv:1010.2799.
- [52] M. Reuter and F. Saueressig, Lect. Notes Phys. **863**, 185 (2013); arXiv:1205.5431.
- [53] P. H. Ginsparg and M. J. Perry, Nucl. Phys. B **222**, 245 (1983).
- [54] R. Bousso and S. W. Hawking, Phys. Rev. D **54**, 6312 (1996); gr-qc/9606052.
- [55] M. S. Volkov and A. Wipf, Nucl. Phys. B **582**, 313 (2000); hep-th/0003081.
- [56] G. Dvali and C. Gomez, arXiv:1005.3497.
- [57] J. L. Cardy, Nucl. Phys. B **270**, 186 (1986).
- [58] A. Shomer, arXiv:0709.3555.
- [59] A. Strominger, JHEP **0110**, 034 (2001); hep-th/0106113.
- [60] A. Bonanno and M. Reuter, Phys. Lett. B **527**, 9 (2002); astro-ph/0106468. A. Bonanno and M. Reuter, Phys. Rev. D **65**, 043508 (2002); hep-th/0106133.
- [61] M. Reuter and H. Weyer, Phys. Rev. D **69**, 104022 (2004); hep-th/0311196.
- [62] M. Reuter and H. Weyer, JCAP **0412**, 001 (2004); hep-th/0410119.
- [63] A. Bonanno, Phys. Rev. D **85**, 081503 (2012); arXiv:1203.1962.
- [64] J. B. Hartle, Gravity, An Introduction to General Relativity, Solutions to Problems, Problem 12.5 (2003); ISBN 0-8053-8663-7 .